Title: Multiscale activity imaging in the mammary gland reveals how oxytocin enables lactation

Authors: Alexander J. Stevenson[1,2†], Gilles Vanwalleghem[3†], Teneale A. Stewart[1,2], Nicholas D. Condon[4], Bethan Lloyd-Lewis[5], Natascia Marino[6,7], James W. Putney[8], Ethan K. Scott[3,9], Adam D. Ewing[1,2], Felicity M. Davis[1,2]*

Affiliations:

[1]Mater Research Institute-The University of Queensland, Faculty of Medicine, The University of Queensland, Brisbane, Queensland, Australia.

[2]Translational Research Institute, Brisbane, Queensland, Australia.

[3]School of Biomedical Sciences, The University of Queensland, Brisbane, Queensland, Australia.

[4]Institute for Molecular Bioscience, The University of Queensland, Brisbane, Queensland, Australia.

[5]Department of Genetics and Developmental Biology, Institut Curie, 75248 Paris, France

[6]Susan G. Komen Tissue Bank at IU Simon Cancer Center, Indianapolis, USA.

[7]Department of Medicine, Indiana University School of Medicine, Indianapolis, USA.

[8]National Institute of Environmental Health Sciences, National Institutes of Health, Research Triangle Park, North Carolina, USA.

[9]Queensland Brain Institute, The University of Queensland, Brisbane, Queensland, Australia.

*Correspondence to: f.davis@uq.edu.au

†Equal contribution

Abstract:

The mammary epithelium is indispensable for the continued survival of more than 5000 mammalian species. For some, the volume of milk ejected in a single day exceeds their entire blood volume. Here, we unveil the spatiotemporal properties of physiological signals that orchestrate milk ejection. Using quantitative, multidimensional imaging of mammary cell ensembles, we reveal how stimulus-evoked Ca^{2+} oscillations couple to contraction in basal epithelial cells. Moreover, we show that Ca^{2+}-dependent contractions generate the requisite force to physically-deform the innermost layer of luminal cells, forcing them to discharge the fluid that they produced and housed. Through the collective action of thousands of these biological positive-displacement pumps, each linked to a contractile ductal network, milk is delivered into the mouth of the dependent neonate, seconds after the command.

One Sentence Summary: This study provides a window into the organization, dynamics and role of epithelial Ca^{2+} responses in the organ principally responsible for sustaining neonatal life in mammals.

Main Text:

The ability to visualize how a single living cell, in its native environment, translates an extracellular message into an intracellular signal to execute a defined task at the cell-level and cooperatively achieve a biological outcome at the organ-level is revolutionizing our understanding of multicellular systems. Such an approach has provided new insights into a range of biological phenomena, including how plants defend against herbivory (*1*), how fish escape looming predators (*2*, *3*) and how mammals store memories (*4*). The rational design and continued refinement of genetically-encoded Ca^{2+} indicators (GECIs) has fueled these advances (*5*). However, the use of GECIs for *in situ* activity mapping in vertebrates, has largely remained an achievement of neuroscience, where neural activity is tightly-coupled to intracellular Ca^{2+} ($[Ca^{2+}]_i$) signaling (*6*). Efforts to map activity networks in specific populations of non-excitable cells in other solid organs is lagging. Our understanding of how epithelial tissues function, for example, has principally arisen through analysis of isolated cells (often serially-propagated under physiologically-extraneous conditions), retrospective examination of fixed tissue and interrogation of genetic knockout

55   models (where biological function is inferred in the absence of physiological redundancy or compensation).

The mammary gland has a universal and indispensable role in mammalian offspring survival. In its functionally-mature state, it consists of an inner layer of luminal (milk-producing) epithelial

60   cells and an outer layer of contractile basal epithelial cells (*7*). When young offspring suckle, maternally-produced oxytocin (OT) binds to its cognate receptor (the OXTR, a G_q-linked G-protein coupled receptor) on mammary basal cells, causing them to contract (*8*). A model, therefore, emerges where activity may be tightly-coupled to $[Ca^{2+}]_i$ in this organ (*8–11*), making functional *in situ* imaging of an epithelial signal-response relationship possible.

65

Here, we engineered mice with directed expression of a GECI to basal epithelial cells in the mammary gland. This enabled us to quantitatively probe the organization and function of real-time $[Ca^{2+}]_i$ signaling events in individual cells within this complex living tissue, at a level of rigor that has only previously been achieved in the adult brain.

70

Basal cell $[Ca^{2+}]_i$ oscillations signal to repetitively deform mammary alveoli and force milk out

We developed transgenic mice that express the fast, ultrasensitive GECI GCaMP6f (*5*) under the inducible control of the cytokeratin (K) 5 gene promoter (*12*) (*GCaMP6f;K5CreERT2* mice) (**Fig.**

75   **1A**). The relatively high baseline fluorescence of this GECI is well-suited for the quantitative assessment of $[Ca^{2+}]_i$ responses in functionally-mature basal cells, which are sparsely distributed with thin cellular processes (*5, 13*) (**Fig. S1**). GCaMP6f consists of a circularly permuted green fluorescent protein (GFP), enabling 3D assessment of its expression and lineage-specific localization using an anti-GFP antibody (*14*) and optimized methods for tissue clearing (*15*).

80   Genetic recombination in this model was high (**Fig. S2**) and showed strong lineage-bias to basal epithelial cells (**Fig. 1B**).

To assess OT-mediated basal cell $[Ca^{2+}]_i$ responses, we performed 4-dimensional (*x*-, *y*-, *z*-, *t*-) quantitative imaging of intact mammary tissue pieces from lactating *GCaMP6f;K5CreERT2* mice.

85   Tissue was loaded with the live-cell permeable dye CellTracker™ Red to visualize alveolar

luminal (milk-producing) cells. A large coordinated wave of $[Ca^{2+}]_i$, likely due to inositol trisphosphate (InsP3)-mediated endoplasmic reticulum (ER) Ca^{2+} store-release (*8*, *9*, *16*), was observed in mammary basal cells following OT stimulation and its diffusion through the tissue (**Fig. 1C** and **Movie S1**). This initial transient $[Ca^{2+}]_i$ elevation was followed by a phase of slow, stochastic $[Ca^{2+}]_i$ oscillations (**Fig. 1C** and **Movie S1**), likely attributable to store-operated Ca^{2+} entry (SOCE) (*9*, *11*).

Increases in $[Ca^{2+}]_i$ appeared to be temporally-correlated with alveolar unit contractions. Whilst cell- and tissue- level movement is physiologically-relevant and important, it poses additional computational challenges to the analysis of single cell Ca^{2+} responses in 4D image sequences. To overcome this, we utilized the diffeomorphic registration approach of Advanced Normalization Tools for motion correction (*17*, *18*). This approach corrected major tissue movements, however, alveolar unit contractions remained intact, enabling quantification of $[Ca^{2+}]_i$ responses in thin basal cells, and analysis of the physical distortions to the alveolar units that these cells embrace. These analyses confirmed that increases in $[Ca^{2+}]_i$ in individual basal cells were temporally correlated with physical distortions to the mechanically-compliant luminal cell layer (**Fig. 1D** and **Fig. S3**). For both the first (InsP3-mediated) response (**Fig. 1E**) and the subsequent oscillatory phase (**Fig. 1F**) increases in $[Ca^{2+}]_i$ preceded alveolar unit contractions. No statistical difference in the firing interval for $[Ca^{2+}]_i$ was observed between the first and second events and all subsequent events (**Fig. 1G**). These results reveal that each mammary alveolar unit, acting downstream of a basal cell OT-OXTR-InsP3-Ca^{2+} signaling axis, serves as a biological positive-displacement pump, repeatedly forcing milk out of its central lumen for passage through the ductal network.

Ca^{2+}-contraction coupling in alveolar basal cells

To directly assess Ca^{2+}-contraction coupling in mammary basal cells, we engineered triple transgenic mice that express GCaMP6f and the red fluorescent protein TdTomato in basal cells (*GCaMP6f-TdTom;K5CreERT2* mice). Using this model, we observed increases in $[Ca^{2+}]_i$ in single TdTomato-positive cells in response to OT, which immediately preceded their contraction (**Fig. 2A-B, Fig. S4A** and **Movie S2**). These data reveal how basal cells contract to deform the inner luminal cell layer for milk ejection and show unequivocally a temporal relationship between the Ca^{2+} signal and the contractile response.

4

The nature of alveolar basal cell contractions was also examined using 3-dimensional, deep-tissue imaging of myosin light chain (MLC) phosphorylation and activation. In OT-treated tissue, phospho-MLC (pMLC) -positive and -negative basal cells were interspersed throughout alveolar clusters (**Fig. 2C**), confirming the phasic and ostensibly-stochastic nature of this response. To determine whether basal contractile responses are truly random or whether there is any evidence for lobuloalveolar cooperativity in firing, we employed two agnostic approaches to analyze the functional connectivity in Ca^{2+} signaling events. First, we analyzed correlations in the firing pattern of individual basal cells in the post-diffusion phase and graphed the Euclidean distances between highly-correlated (> 0.5) cells. Highly-correlated responses exhibited a short Euclidean distance (**Fig. 2D**). Next, we analyzed network topologies by connecting highly-correlated cells within a single field-of-view. This method confirmed high clustering associated with short internodal distances in some lobular structures (small-worldness) (**Fig. S4B**) (*19, 20*). These analyses suggest some cooperativity in firing and, by extension, contraction. An important caveat of this model, however, is the constant, uniform application of OT in the bath. Physiologically, the picture is likely to be more complex, due to pulsatile bursts of OT from oxytocinergic neurons in response to infant suckling (*8*). Platforms to measure, in high resolution, single cell $[Ca^{2+}]_i$ responses in conscious and actively-feeding mice, with normal maternal and social behaviors, have not yet been optimally developed.

Basal cells upregulate their contractile machinery during gestation and are licensed-to-respond to $[Ca^{2+}]_i$ oscillations

Our quantitative image analysis revealed a two-component (signal-response) model of milk ejection, involving a GPCR-InsP3-Ca^{2+} signaling component linked to a contractile actin-myosin network. This prompted us to investigate developmental stage-specific variations to this model. To assess $[Ca^{2+}]_i$ responses in mammary epithelial cells from non-pregnant mice, we created mammary organoids (*21*). An organoid model (retaining key structural (**Fig. S5**) and functional (*21*) features of the *in vivo* non-pregnant gland) was utilized in this context to overcome limitations associated with resolving single-cell $[Ca^{2+}]_i$ responses in epithelial structures embedded deep within a light-scattering fat pad (**Fig. S6**). OT-stimulation of mammary organoids isolated from

virgin *GCaMP6f;K5CreERT2* mice produced $[Ca^{2+}]_i$ oscillations in basal cells (**Fig. 3A and Movie S3**). However, $[Ca^{2+}]_i$ oscillations were uncoupled to contraction in this model (**Fig. 3B**).

To investigate how this signal-response relationship may be uncoupled in the non-pregnant state, we analyzed single-cell RNA sequencing data from cells isolated from mammary glands of nulliparous, pregnant, lactating and involuting mice (*22*). Unsupervised clustering has previously revealed four populations of cells with a basal profile, which strongly correlates with the developmental stage of isolation (*22*). Comparing the "Basal-Virgin" and "Basal-Lac" clusters exposed a high number of differentially-expressed genes (**Fig. 3C**). The Basal-Lac cluster was significantly enriched for genes in the vascular smooth muscle contraction pathway (**Fig. 3D**), including myosin light chain kinase (*Mylk*), calponin (*Cnn1*) and caldesmon (*Cald1*) (**Fig. 3E**). These findings were validated by immunostaining (**Fig. 3F** and **Fig. S7**).

Both ducts and alveoli contract to expel milk in the mature gland

The lactating mouse mammary gland consists of milk-producing alveoli that are connected to the nipple via a branching ductal network. Heterogeneity in the expression of contractile markers in basal cells of ducts and alveoli has led to speculation that these two spatially-distinct cell populations are functionally-divergent (*23*). Immunohistochemical analysis of MYLK, CNN1 and CALD1 in small ducts, large ducts and alveoli of lactating mice (**Fig. 4A**) and humans (**Fig. 4B**) revealed that these contractile proteins are expressed at comparable levels in ducts and alveoli. We therefore examined Ca^{2+}-contraction coupling in ductal cells of *GCaMP6f-TdTom;K5CreERT2* mice at day 15.5-16.5 gestation (dpc). At this developmental stage, contractile proteins are already upregulated (**Fig. 3E**), Ca^{2+}-contraction coupling is observed in alveolar structures (**Movie S4**) and the visualization of ducts is not encumbered by light scattering and/or absorptive properties of interposing structures. Ca^{2+}-contraction coupling was clearly observed in ductal basal cells (**Fig. 4C** and **Movie S5**). On one occasion, a large duct from a lactating animal was able to be visualized at high cellular resolution (**Movie S6**), confirming these findings in the fully-mature state.

In ducts, basal cells adopt a spindle like morphology and are collectively-oriented along the length of the duct. Our data reveal that contraction of these cells generates longitudinal motion, facilitating the continued flow of milk. We also definitively demonstrate that differences in the

6

type of motion generated by ductal and alveolar contractions stem from organizational heterogeneity—rather than divergent functional differentiation or signal transduction—resolving a longstanding unanswered question in the field.

Basal cell contractions are calcium-signal dependent with "loose" coupling

We used pharmacological tools to interrogate intracellular pathways that may be involved in Ca^{2+}-contraction coupling in mammary basal cells. Cells from *GCaMP6f-TdTom;K5CreERT2* (15.5-16.5 dpc) mice were isolated, plated in co-culture on a nanopatterned surface (**Fig. 5A**) and imaged within 12 h of dissection. These conditions were optimal for: *1*) maintaining cell health and stage-specific differentiation, and *2*) achieving anisotropy in the arrangement of contractile elements for the experimental measurement of force-generation along a single axis (*24*). Under these conditions, OT stimulation produced $[Ca^{2+}]_i$ responses, which were coupled to contraction at the first (InsP3) phase (**Fig. 5B-C** and **Movie S7**). Later phase Ca^{2+}-contraction coupling was not able to be assessed in this model, due to the intensity of the first contraction (even at pM concentrations of OT) and the relatively low strength of the newly-formed surface adhesions. Nevertheless, as Ca^{2+}-contraction coupling is observed at this phase (**Fig. 1D-E** and **Fig. 2A-B**), the model is fit.

Intracellular Ca^{2+} chelation with BAPTA completely blocked $[Ca^{2+}]_i$ responses to OT (**Fig. 5C and Movie S8**). Cell contractions were also blocked (**Fig. 5C and Movie S8**) demonstrating, unequivocally, their Ca^{2+}-dependence. To gauge the distance between the Ca^{2+} source (in this case InsP3 receptors) and sensor, we compared OT-mediated basal cell contractions in cells loaded with two different $[Ca^{2+}]_i$ chelators (BAPTA-AM and EGTA-AM), with different Ca^{2+} binding rates but comparable binding affinities (*25*, *26*). Both intracellular BAPTA and EGTA were able to capture Ca^{2+} between the channel and the sensor (**Fig 5C**), suggestive of "loose" Ca^{2+}-contraction coupling in these cells that is not strictly dependent on nanodomain signaling (*26*). Inhibition of the Ca^{2+}/calmodulin-dependent MYLK (with ML-7), rho-associated protein kinase (with Y27632) or dual inhibition (ML-7 + Y27632) (*27*) failed to block OT-mediated basal cell contraction in this model (**Fig 5C**). These data suggest that, similar to vascular smooth muscle cells (*28*), MYLK-independent contractile pathways can also operate in functionally-mature mammary basal cells.

Distinct signaling pathways underpin the passage of milk, tears and sperm

7

To assess potential conservation in the signaling pathways that operate in basal cells of other OT-sensitive, fluid-transporting epithelia, we assessed OT-mediated responses in the lacrimal glands and epididymides of *GCaMP6f-TdTom;K5CreERT2* mice. In the lacrimal gland, basal cells have a similar morphology, arrangement and function to mammary basal cells (*29*). They have previously been shown to undergo OT-dependent contractions (*30*), and diminished OT-OXTR signaling in these cells has been linked to dry eye disease (*30*). Like the mammary gland, dual expression of basal and smooth muscle markers was confirmed in lacrimal acini (**Fig. 6A**), however, no OT-mediated $[Ca^{2+}]_i$ or contractile responses were detected in these cells in this study (**Fig. 6B-C** and **Movie S9**).

In males, a large burst of OT is released into the bloodstream at ejaculation (*8, 31*). This produces contractions of the male reproductive tract and, by assisting with the passage of fluid along this tract, these contractions are thought to reduce post-ejaculatory refractoriness and improve reproductive readiness (*31, 32*). Epididymal basal cells express basal cell markers, however, unlike the lacrimal and mammary glands, they do not co-express smooth muscle markers (**Fig. 6D**). Instead, movement of fluid through this organ appears to rely on a layer of smooth muscle surrounding the inner tubular epithelium (**Fig. 6D**). To assess the transport of sperm through this organ, its OT-responsiveness and its relationship to basal cell $[Ca^{2+}]_i$ elevations, we stimulated intact epididymal tissue with a large bolus dose of OT. OT stimulation triggered marked peristaltic-like movements of the epididymal tubes (**Fig. 6E**) and a supra-basal pattern of phosphorylation of MLC (**Fig. S8**). Low frequency Ca^{2+} firing in basal cells was observed before and after OT-stimulation (**Fig. 6F** and **Movie S10**). Ca^{2+}-contraction signaling can therefore be selectively uncoupled in different fluid-moving, stratified epithelia, either by variation of the signal, source or sensor.

Discussion

Real-time, *in situ* activity monitoring provides important insights into how individual cells behave in multi-dimensional and multi-cellular environments (*1–4*). This approach was used to describe and quantify the mechanism by which milk is transported through the mammary epithelium, making it available on-demand and with minimal delay to the nursing neonate (*8, 33*). Our data support four novel findings. Firstly, we revealed that transient $[Ca^{2+}]_i$ elevations precede and are

240 required for basal cell contractions in the functionally-mature mammary gland. We extended this finding to demonstrate how Ca^{2+}-contraction coupling in a single basal cell can physically warp the layer of alveolar luminal cells that it encircles. Through this repetitive and collective (although not highly-coordinated) effort, large volumes of a thick biological emulsion can be forced through a narrow passage in a manner that is both consistent and persistent. Structure, function and
245 expression were examined in the adjoining ductal epithelium, previously relegated to a role akin to a biological drinking straw. Instead, these analyses revealed active participation of the ductal epithelium in the process of milk ejection. Differences in the motion generated by basal cell contractions in ducts and alveoli could be ascribed to heterogeneity in cellular organization, rather than expression or function of contractile elements. Finally, we compared mammary, lacrimal and
250 epididymal tissue in 4-dimensions, highlighting how these resembling structures utilize divergent pathways to optimally propel their biological fluid out of the mammalian body.

References

1. M. Toyota *et al.*, Glutamate triggers long-distance, calcium-based plant defense signaling. *Science*. **361**, 1112–1115 (2018).
255
2. L. A. L. Heap, G. Vanwalleghem, A. W. Thompson, I. A. Favre-Bulle, E. K. Scott, Luminance changes drive directional startle through a thalamic pathway. *Neuron*. **99**, 293–301 (2018).

3. T. W. Dunn *et al.*, Neural circuits underlying visually evoked escapes in larval zebrafish.
260 *Neuron*. **89**, 613–628 (2016).

4. J. Cichon, W. B. Gan, Branch-specific dendritic Ca2+ spikes cause persistent synaptic plasticity. *Nature*. **9**, 180–5 (2015).

5. T.-W. Chen *et al.*, Ultrasensitive fluorescent proteins for imaging neuronal activity. *Nature*. **499**, 295–300 (2013).
265
6. Q. Chen *et al.*, Imaging neural activity using Thy1-GCaMP transgenic mice. *Neuron*. **76**, 297–308 (2012).

7. B. Lloyd-Lewis, O. B. Harris, C. J. Watson, F. M. Davis, Mammary stem cells: Premise, properties and perspectives. *Trends Cell Biol*. **8**, 556–567 (2017).

8. G. Gimpl, F. Fahrenholz, The oxytocin receptor system: structure, function, and
270 regulation. *Physiol. Rev*. **81**, 629–683 (2001).

9.   F. M. Davis *et al.*, Essential role of Orai1 store-operated calcium channels in lactation. *Proc. Natl. Acad. Sci.* **112**, 5827–5832 (2015).

10.   D. M. Moore, A. W. Vogl, K. Baimbridge, J. T. Emerman, Effect of calcium on oxytocin-induced contraction of mammary gland myoepithelium as visualized by NBD-phallacidin. *J. Cell Sci.* **88**, 563–569 (1987).

11.   G. M. Olins, R. D. Bremel, Oxytocin-stimulated myosin phosphorylation in mammary myoepithelial cells: Roles of calcium ions and cyclic nucleotides. *Endocrinology*. **114**, 1617–1626 (1984).

12.   A. Van Keymeulen *et al.*, Distinct stem cells contribute to mammary gland development and maintenance. *Nature*. **479**, 189–193 (2011).

13.   H. Dana *et al.*, High-performance GFP-based calcium indicators for imaging activity in neuronal populations and microcompartments. *bioRxiv*, 434589 (2018).

14.   R. Srinivasan *et al.*, New transgenic mouse lines for selectively targeting astrocytes and studying calcium signals in astrocyte processes in situ and in vivo. *Neuron*. **92**, 1181–1195 (2016).

15.   B. Lloyd-Lewis *et al.*, Imaging the mammary gland and mammary tumours in 3D: Optical tissue clearing and immunofluorescence methods. *Breast Cancer Res.* **18** (2016).

16.   H. Nakano, K. Furuya, S. Yamagishi, Synergistic effects of ATP on oxytocin-induced intracellular Ca2+ response in mouse mammary myoepithelial cells. *Pflugers Arch. Eur. J. Physiol.* **442**, 57–63 (2001).

17.   B. B. Avants *et al.*, A reproducible evaluation of ANTs similarity metric performance in brain image registration. *Neuroimage*. **54**, 2033–44 (2011).

18.   B. B. Avants, C. Epstein, M. Grossman, J. C. Gee, Symmetric diffeomorphic image registration with cross-correlation: evaluating automated labeling of elderly and neurodegenerative brain. *Med. Image Anal.* **12**, 26–41 (2008).

19.   A. Stožer *et al.*, Functional connectivity in islets of Langerhans from mouse pancreas tissue slices. *PLoS Comput. Biol.* **9**, e1002923 (2013).

20.   D. J. Watts, S. H. Strogatz, Collective dynamics of "small-world" networks. *Nature*. **393**, 440–2 (1998).

21.   T. Jarde *et al.*, Wnt and Neuregulin1/ErbB signalling extends 3D culture of hormone responsive mammary organoids. *Nat. Commun.* **7**, 13207 (2016).

22. K. Bach *et al.*, Differentiation dynamics of mammary epithelial cells revealed by single-cell RNA sequencing. *Nat. Commun.* **8** (2017).

23. M. Moumen *et al.*, The mammary myoepithelial cell. *Int. J. Dev. Biol.* (2011).

24. S. Chaterji *et al.*, Synergistic effects of matrix nanotopography and stiffness on vascular smooth muscle cell function. *Tissue Eng. Part A*. **20**, 2115–26 (2014).

25. N. P. Vyleta, P. Jonas, Loose coupling between Ca2+ channels and release sensors at a plastic hippocampal synapse. *Science*. **343**, 665–70 (2014).

26. E. Eggermann, I. Bucurenciu, S. P. Goswami, P. Jonas, Nanodomain coupling between Ca 2+ channels and sensors of exocytosis at fast mammalian synapses. *Nat. Rev. Neurosci.* **13**, 7–21 (2012).

27. K. Raymond *et al.*, Control of mammary myoepithelial cell contractile function by α3β1 integrin signalling. *EMBO J.* **30**, 1896–1906 (2011).

28. A. V. Somlyo *et al.*, Myosin Light Chain Kinase Knockout. *J. Muscle Res. Cell Motil.* (2004).

29. D. T. Farmer *et al.*, Defining epithelial cell dynamics and lineage relationships in the developing lacrimal gland. *Development*. **144**, 2517–2528 (2017).

30. D. Hawley *et al.*, Myoepithelial cell-driven acini contraction in response to oxytocin receptor stimulation is impaired in lacrimal glands of Sjögren's syndrome animal models. *Sci. Rep.* **8**, 9919 (2018).

31. H. Thackare, H. D. Nicholson, K. Whittington, Oxytocin - Its role in male reproduction and new potential therapeutic uses. *Hum. Reprod. Update*. **12**, 437–48 (2006).

32. S. Arrighi, Are the basal cells of the mammalian epididymis still an enigma? *Reprod. Fertil. Dev.* **26**, 1061–71 (2014).

33. C. J. Watson, W. T. Khaled, Mammary development in the embryo and adult: a journey of morphogenesis and commitment. *Development*. **135**, 995–1003 (2008).

34. M. E. Sherman *et al.*, The Susan G. Komen for the Cure Tissue Bank at the IU Simon Cancer Center: A unique resource for defining the "molecular histology" of the breast. *Cancer Prev. Res.* **5**, 528–535 (2012).

35. F. M. Davis *et al.*, Single-cell lineage tracing in the mammary gland reveals stochastic clonal dispersion of stem/progenitor cell progeny. *Nat. Commun.* **7**, 13053 (2016).

36. E. A. Susaki *et al.*, Whole-brain imaging with single-cell resolution using chemical

cocktails and computational analysis. *Cell*. **157**, 726–39 (2014).

37. B. Lloyd-Lewis, F. M. Davis, O. B. Harris, J. R. Hitchcock, C. J. Watson, Neutral lineage tracing of proliferative embryonic and adult mammary stem/progenitor cells. *Development*. **145**, dev164079 (2018).

38. M. Linkert *et al.*, Metadata matters: access to image data in the real world. *J. Cell Biol.* **189** (2010), pp. 777–782.

39. J. Schindelin *et al.*, Fiji: an open source platform for biological image analysis. *Nat. Methods*. **9**, 676–682 (2012).

40. J. Boulanger *et al.*, Patch-based nonlocal functional for denoising fluorescence microscopy image sequences. *IEEE Trans. Med. Imaging*. **29**, 442–54 (2010).

41. M. Prater, M. Shehata, C. J. Watson, J. Stingl, Enzymatic dissociation, flow cytometric analysis, and culture of normal mouse mammary tissue. *Methods Mol.Biol.* **946**, 395–409 (2013).

42. H. Jia, N. L. Rochefort, X. Chen, A. Konnerth, In vivo two-photon imaging of sensory-evoked dendritic calcium signals in cortical neurons. *Nat. Protoc.* **6**, 28–35 (2011).

43. A. Giovannucci *et al.*, CaImAn an open source tool for scalable calcium imaging data analysis. *Elife*. **8**, e38173 (2019).

44. M. D. Robinson, D. J. McCarthy, G. K. Smyth, edgeR: A Bioconductor package for differential expression analysis of digital gene expression data. *Bioinformatics*. **26**, 139–40 (2009).

45. M. Waskom *et al.*, mwaskom/seaborn: v0.9.0 (July 2018) (2018).

46. A. Subramanian *et al.*, Gene set enrichment analysis: A knowledge-based approach for interpreting genome-wide expression profiles. *Proc. Natl. Acad. Sci.* **102**, 15545–15550 (2005).

12

Main figures and figure legends

13

Fig. 1

A K5-CreERT2 / CreERT2 expressed in basal cells X GCaMP6f-fl / Fast GECI induced by Cre — Basal cell, GCaMP6f+

B *GCaMP6f;K5CreERT2* (mammary gland) — Max. intensity projection — GFP/GCaMP6f SMA 100 μm

C OT — Live *ex vivo* lactating mammary tissue *(GCaMP6f;K5CreERT2 mice)* — CellTracker™ GCaMP6f 100 μm

D Basal cell [Ca²⁺]ᵢ; Alveolar contraction

E, F Relative *t* (s) from peak Ca²⁺
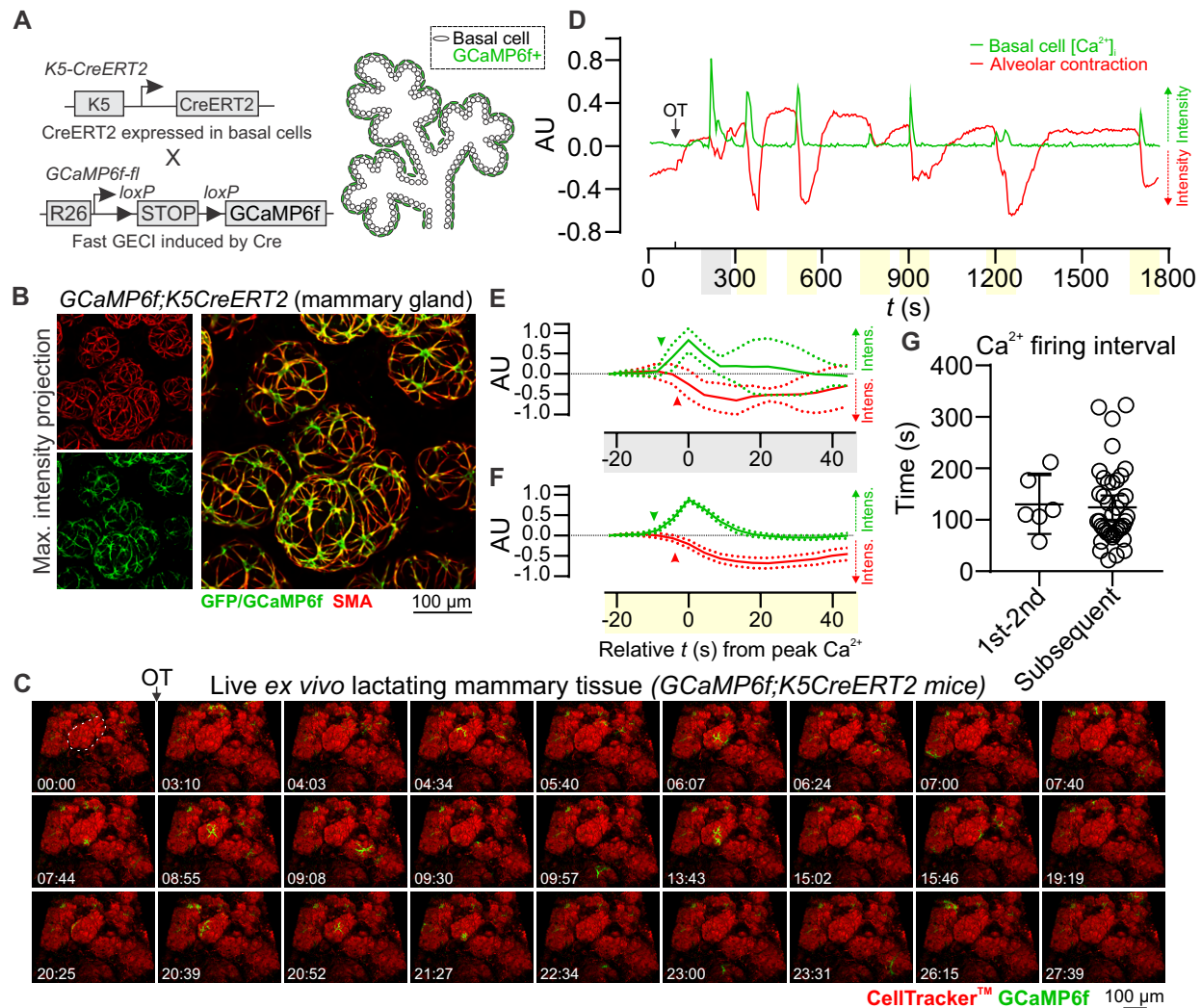
G Ca²⁺ firing interval

Fig. 1. Basal cell Ca^{2+} oscillations precede alveolar contractions in lactation. (**A**) Schematic representation of the *GCaMP6f;K5CreERT2* model. (**B**) Maximum intensity *z*-projection (0-60 μm) of cleared lactating mammary tissue immunostained with smooth muscle actin (SMA) to reveal basal cells and an anti-GFP antibody to detect GCaMP6f expression (n = 3 mice). (**C**) 3D time-lapse imaging of live mammary tissue from *GCaMP6f;K5CreERT2* lactating mice stimulated with OT (85 nM) at 01:33 (min:s). Images show maximum intensity *z*-projection 32 μm through live tissue; dotted line (frame 1) identifies a single alveolar unit. (**D**) [Ca^{2+}]$_i$ responses (green) and alveolar unit contraction (red) in lactating mammary tissue from *GCaMP6f;K5CreERT2* mice. [Ca^{2+}]$_i$ measurements are ΔF/F$_0$. Alveolar unit contractions are shown by negative deflections (CellTracker™ fluorescence). (**E-F**) Average (± SEM) peak [Ca^{2+}]$_i$ and contractile responses. Highlighting (x-axis) corresponds with events linked in D; arrowheads show initiation of response; n = 3 mice. (**G**) Interval between the first-second and all subsequent [Ca^{2+}]$_i$ events; n = 3 mice. AU, arbitrary unit.

14

Fig. 2

A OT Live *ex vivo* lactating mammary tissue (*GCaMP6f-TdTom;K5CreERT2* mice)

TdTomato GCaMP6f 100 μm

B

— Basal cell [Ca²⁺]
— Basal cell contraction

C Max. intensity projection

No stimulation   Oxytocin
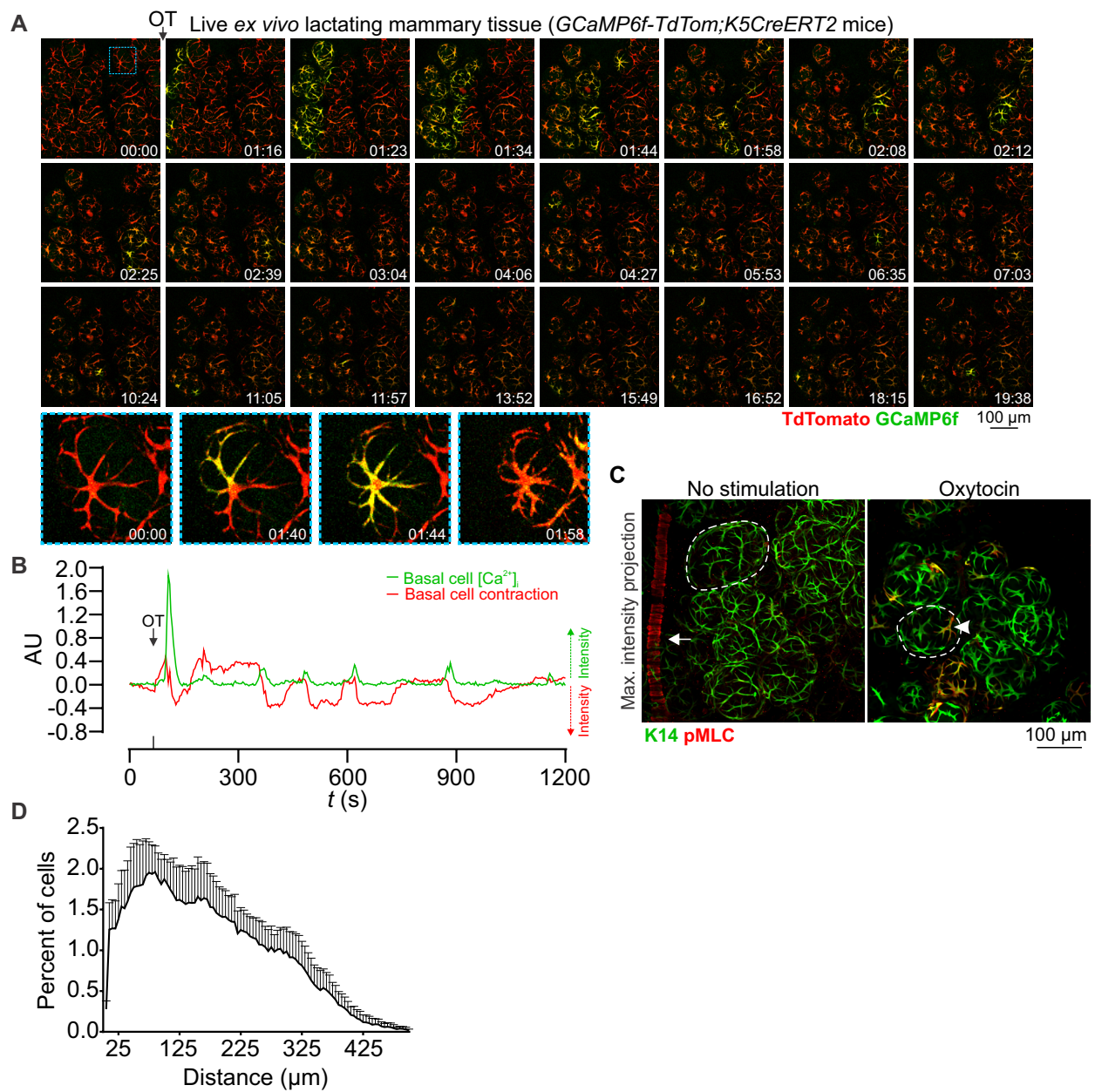
K14 pMLC   100 μm

D

Fig. 2. Ca²⁺-contraction coupling in alveolar basal cells. (**A**) 3D time-lapse imaging of live
400   mammary tissue from *GCaMP6f-TdTom;K5CreERT2* mice stimulated with OT (85 nM) at 01:09 (min:s). Images show maximum intensity *z*-projection (31.5 μm). Box (frame 1) is expanded below. (**B**) $[Ca^{2+}]_i$ responses (green) and alveolar unit contraction (red) in lactating mammary tissue from *GCaMP6f-TdTom;K5CreERT2* mice. $[Ca^{2+}]_i$ measurements are $\Delta F/F_0$. Basal cell contractions are shown by negative deflections (TdTomato fluorescence). (**C**) Maximum intensity
405   *z*-projections [0-120 μm (left), 0-44 μm (right)] of cleared mammary tissue immunostained with K14 to reveal basal cells and pMLC to show contractile activity. Arrow shows pMLC+ blood vessel in control mammary tissue (lactation), arrowhead shows pMLC+ basal cell in lactating mammary tissue stimulated with OT (85 nM) immediately prior to fixation; dotted lines surround single alveolar units in each image (n = 3 mice). (**D**) Percent of cells with a high correlation
410   coefficient (> 0.5) in Ca^{2+} firing and the Euclidean distance from correlated events. Graph shows average ± SEM (n = 4 mice, gestation). AU, arbitrary unit.
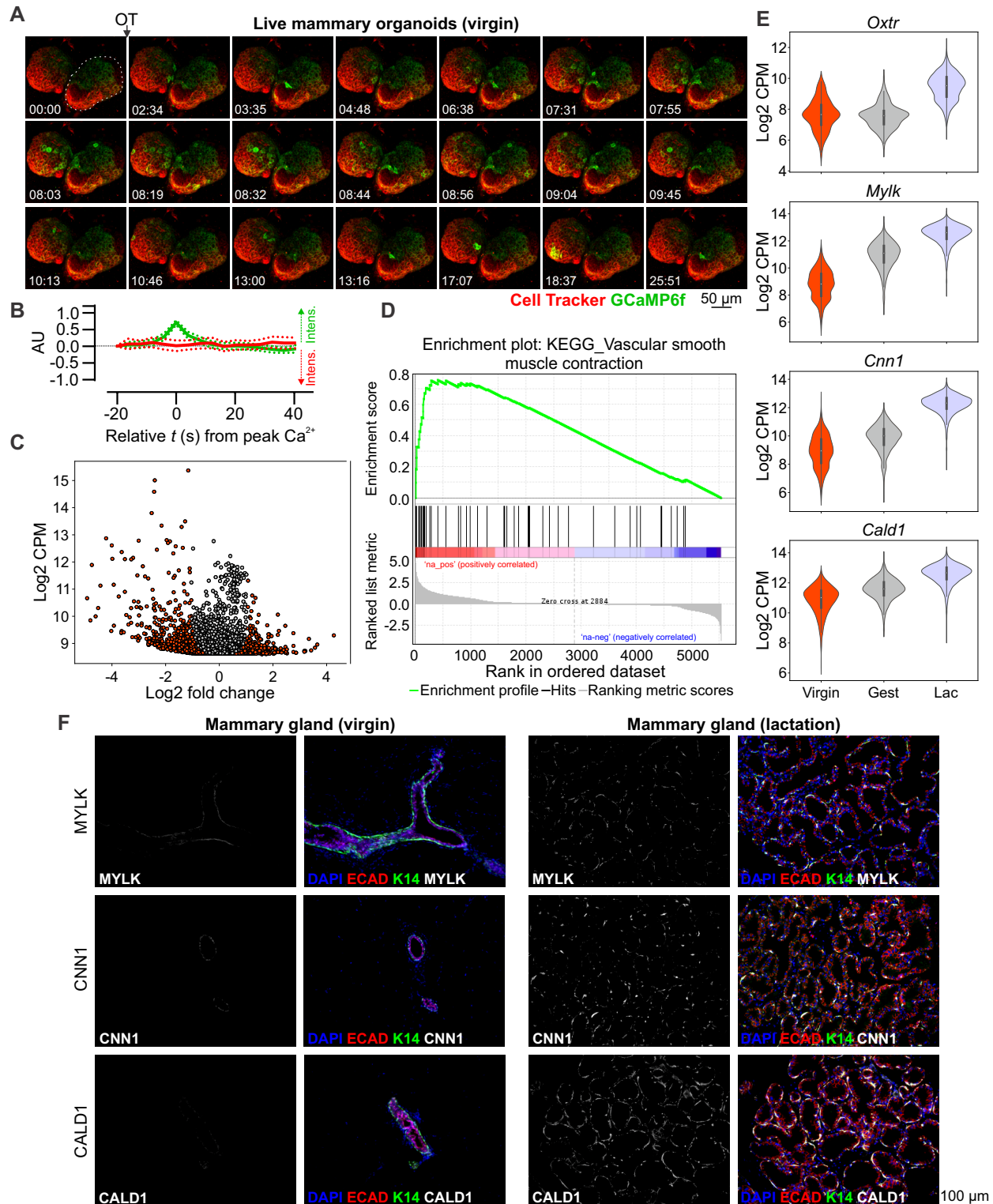
15

Fig. 3

A Live mammary organoids (virgin)

Cell Tracker GCaMP6f 50 µm

B

C

D Enrichment plot: KEGG_Vascular smooth muscle contraction

−Enrichment profile −Hits −Ranking metric scores

E *Oxtr* *Mylk* *Cnn1* *Cald1*

Virgin Gest Lac

F Mammary gland (virgin)   Mammary gland (lactation)

MYLK   CNN1   CALD1

100 µm

Fig. 3. Upregulation of the contraction toolkit in basal cells during pregnancy and lactation.

415   (**A**) 3D time-lapse imaging of live mammary organoids prepared from non-pregnant (virgin) *GCaMP6f;K5CreERT2* mice. Organoids were stimulated with OT (85 nM). Image series show maximum intensity *z*-projection 52 μm through organoid structure; dotted line (frame 1) reveals a single organoid; n = 3 mice. (**B**) Average (± SEM) peak $[Ca^{2+}]_i$ and contractile responses (first and second phase). $[Ca^{2+}]_i$ measurements (green) are $\Delta F/F_0$. Organoid movements (red, CellTracker™

420   fluorescence). (**C**) Volcano plot showing differential expression (red dots; FDR < 0.05) from single-cell RNA sequencing data (Basal-Virgin vs. Basal-Lac clusters). (**D**) Genes in the KEGG vascular smooth muscle contraction pathway showed significant enrichment in Basal-Lac vs. Basal-Virgin by GSEA using MSigDB curated gene sets. (**E**) Frequency distribution of expression values from Basal-Virgin, Basal-Gest (gestation) and Basal-Lac clusters shown as a violin plot for

425   each gene. Expression (y-axis) shown as log2 counts per million (CPM); width reflects the distribution of values on the y-axis. (**F**) Immunohistochemical staining for myosin light chain kinase (MYLK), calponin (CNN1) and caldesmon (CALD1) in mammary tissue isolated from virgin and lactating wild-type mice. E-cadherin (red) shows the luminal cell lineage; K14 (green) shows the basal cell lineage. Nuclei are stained with DAPI (blue); n = 3 mice. AU, arbitrary unit.
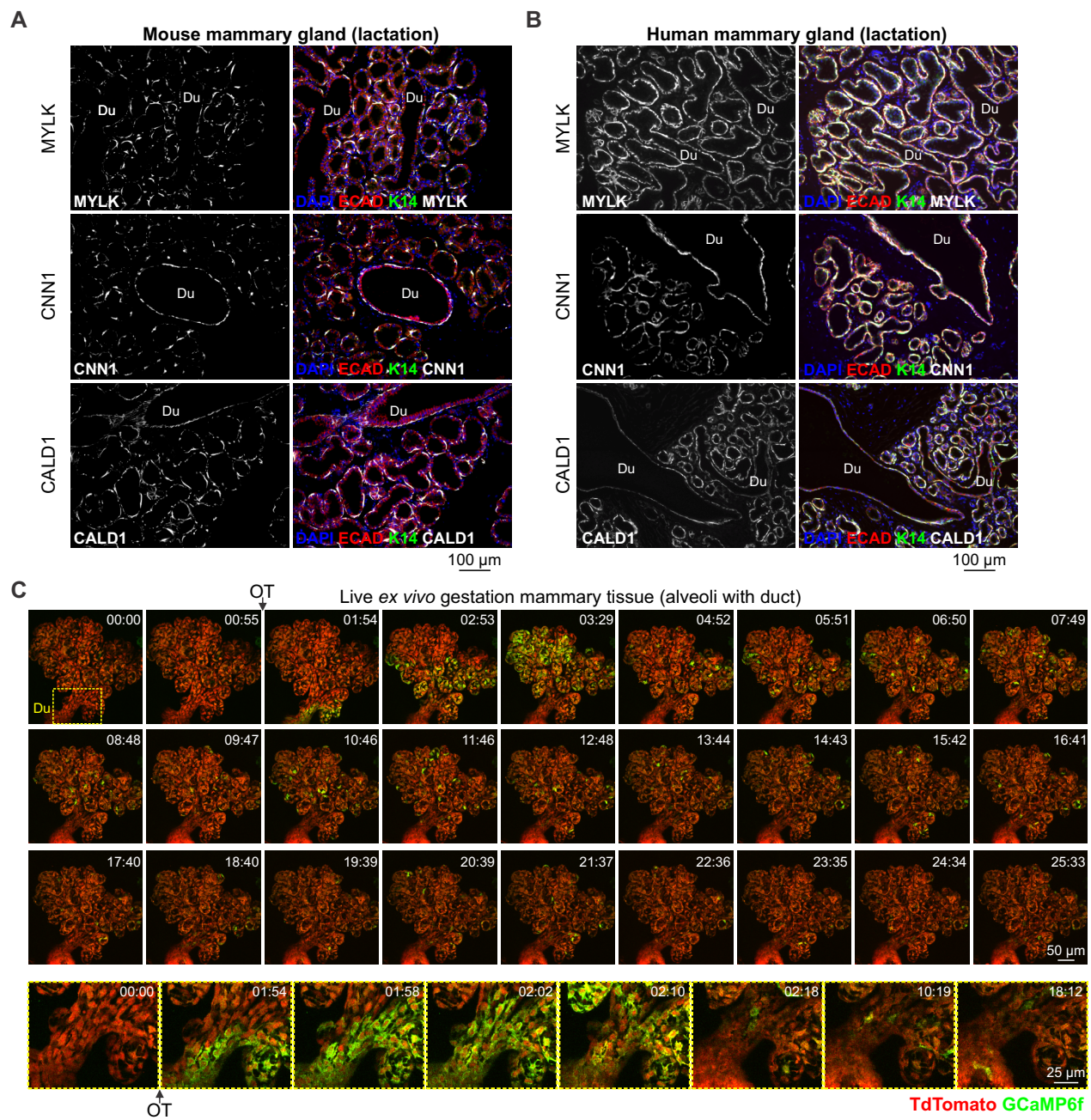
430

Fig. 4

Fig. 4. Functional differentiation and Ca^{2+}-contraction coupling in ducts and alveoli. (**A-B**) Immunostaining of mouse and human lactating tissue. MYLK, CNN1 and CALD1 are expressed in both ducts (Du) and alveoli. E-cadherin (red) shows the luminal cell lineage; K14 (green) shows the basal cell lineage. Nuclei are stained with DAPI (blue); n = 3 samples, mouse and human. (**C**) 3D time-lapse imaging of live mammary tissue from a pregnant (15.5 dpc) *GCaMP6f-TdTom;K5CreERT2* mouse stimulated with OT (85 nM) at 01:15 (min:s). Images show maximum intensity *z*-projection of 45 μm of live tissue; box (frame 1) shows subtending duct (magnified in bottom panel); n = 3 mice.
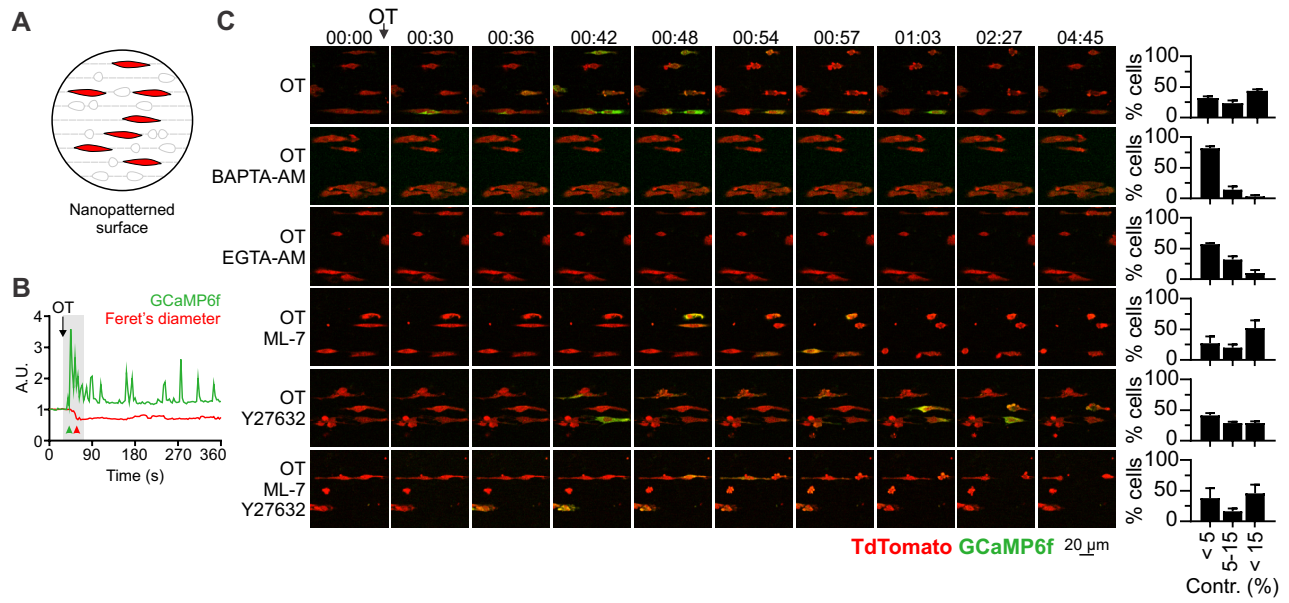
Fig. 5

445

450

Fig. 5. Basal cell contractions are Ca^{2+} signal dependent. (**A**) Schematic representation of the assay developed to assess contractile responses of functionally-differentiated primary basal cells. Basal cells isolated from *GCaMP6f-TdTom;K5CreERT2* mice at late gestation express GCaMP6f and TdTomato. (**B**) First phase (gray box) Ca^{2+}-contraction coupling in primary cells. (**C**) 2D time-lapse imaging of GCaMP6f-TdTomato dual positive cells in response to OT (0.85 nM, 00:27), or with OT in cells loaded with the intracellular Ca^{2+} chelators (BAPTA-AM and EGTA-AM), myosin light chain kinase inhibitor (ML-7), Rho-associated protein kinase inhibitor (Y27632) or a combination of ML-7 and Y27632. Graphs show average (± SEM) percent cells in each bin [<5%, 5-15%, >15% reduction in Feret's diameter (contr.)]; 80-150 cells analyzed for each treatment from n = 3 mice.
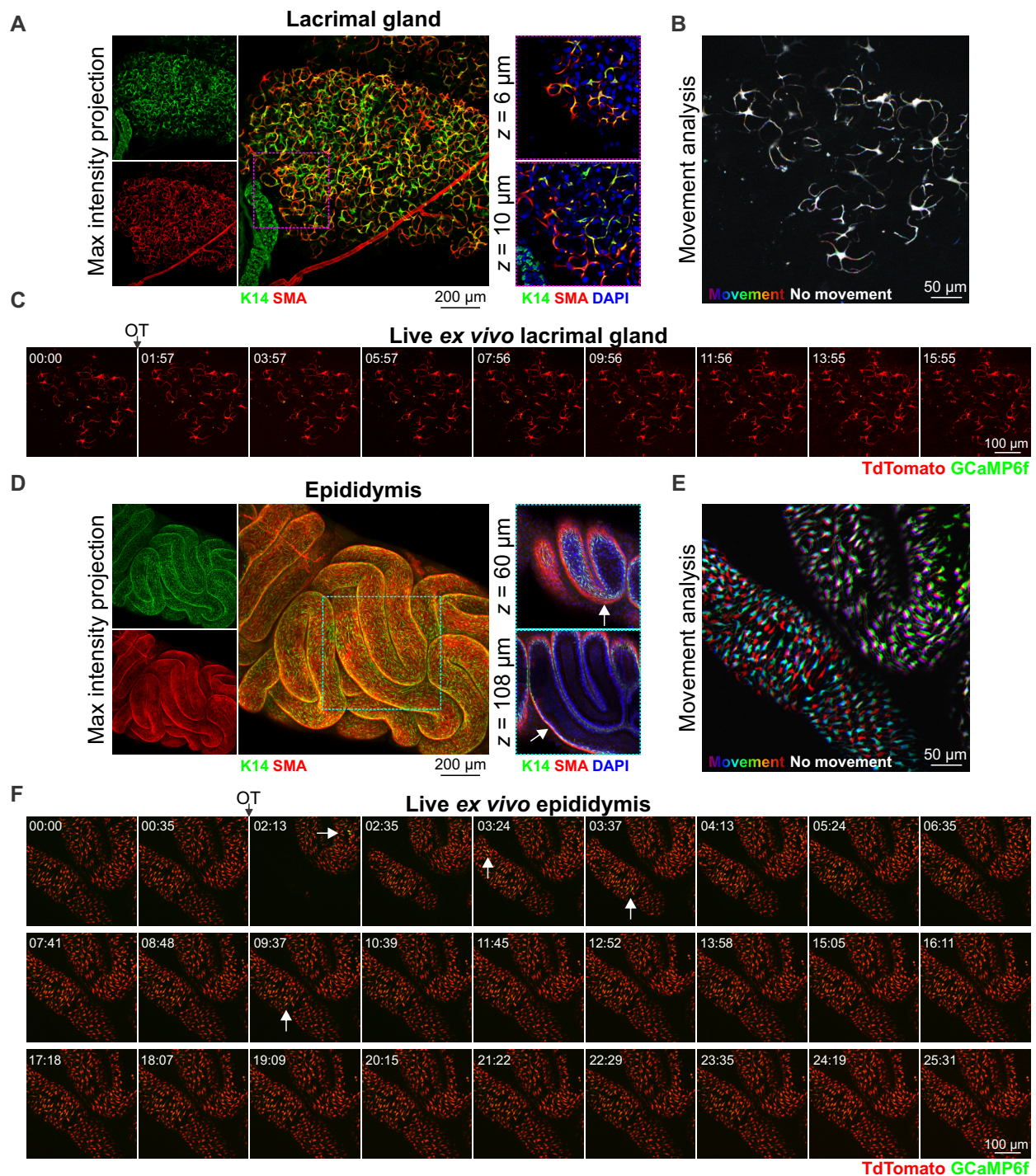
18

Fig. 6

A — **Lacrimal gland** — Max intensity projection — z = 6 µm, z = 10 µm — K14 SMA — 200 µm — K14 SMA DAPI

B — Movement analysis — Movement No movement — 50 µm

C — OT — **Live *ex vivo* lacrimal gland** — 00:00, 01:57, 03:57, 05:57, 07:56, 09:56, 11:56, 13:55, 15:55 — 100 µm — TdTomato GCaMP6f

D — **Epididymis** — Max intensity projection — z = 60 µm, z = 108 µm — K14 SMA — 200 µm — K14 SMA DAPI

E — Movement analysis — Movement No movement — 50 µm

F — OT — **Live *ex vivo* epididymis** — 00:00, 00:35, 02:13, 02:35, 03:24, 03:37, 04:13, 05:24, 06:35 — 07:41, 08:48, 09:37, 10:39, 11:45, 12:52, 13:58, 15:05, 16:11 — 17:18, 18:07, 19:09, 20:15, 21:22, 22:29, 23:35, 24:19, 25:31 — 100 µm — TdTomato GCaMP6f

Fig. 6. OT responses in basal epithelial cells of other fluid-moving organs. (**A**) Maximum intensity *z*-projection (0-36 μm) and optical slices of lacrimal tissue. Lacrimal acinar basal cells express K14 and SMA (n = 3 mice). (**B**) Analysis of tissue movement created by the overlay of 3 images (each 43 s apart). Each image has been assigned a primary color (R-G-B). Regions that do not move during the 90 s window have R-G-B pixels superimposed and are white. Regions where significant movement has occurred appear R, G, B or a combination of 2 colors. (**C**) 3D time-lapse imaging of lacrimal tissue from *GCaMP6f-TdTom;K5CreERT2* mice. Tissue was stimulated with OT (85 nM, 00:45). Image series show maximum intensity *z*-projection (21 μm); n = 3 mice. (**D**) Maximum intensity *z*-projection (0-246 μm) and optical slices of cleared mouse epididymis (caput). Basal K14 positive cells are surrounded by SMA positive cells (arrow) (n = 3 mice). (**E**) Tissue movement analysis of 3 images (45 s apart) as per (B). (**F**) 3D time-lapse imaging of epididymal tissue from *GCaMP6f-TdTom;K5CreERT2* mice. Tissue was stimulated with OT (850 nM, 01:38); arrows show single cell calcium responses. Series is maximum intensity *z*-projection 104.5 μm through the structure; n = 3 mice.

470

19

Supplementary Materials for

Calcium oscillations control lactation

Alexander J. Stevenson[†], Gilles Vanwalleghem[†], Teneale A. Stewart, Nicholas D. Condon, Bethan Lloyd-Lewis,
Natascia Marino, James W. Putney, Ethan K. Scott, Adam D. Ewing, Felicity M. Davis
[†]Equal contribution

Correspondence to: f.davis@uq.edu.au

This PDF file includes:

>   Materials and Methods
>   Figs. S1 to S8
>   Captions for Movies S1 to S10

Other Supplementary Materials for this manuscript include the following:

>   Movies S1 to S10
>   Key Resources Table

Materials and Methods

<u>Mice</u>

Animal experimentation was carried out in accordance with the *Australian Code for the Care and Use of Animals for Scientific Purposes* and the *Queensland Animal Care and Protection Act (2001)*, with local animal ethics committee approval. Animals were kept in a Specific Pathogen Free facility under a 12:12 h light-dark cycle in individually-ventilated cages. Food and water were available *ad libitum* and standard enrichment provided. All strains were purchased and maintained on a C57BL6/J background. *K5CreERT2* mice (B6N.129S6(Cg)-Krt5$^{tm1.1(cre/ERT2)Blh}$/J, stock no. 029155) were purchased from The Jackson Laboratory (Bar Harbor, ME) and maintained as heterozygotes. *TdTomato-fl* mice (B6.Cg-*Gt(ROSA)26Sor*$^{tm9(CAG-tdTomato)Hze}$/J, stock no. 007909) were a kind gift from Prof. Ian Frazer (University of Queensland). *GCaMP6f-fl* mice (B6J.Cg-*Gt(ROSA)26Sor*$^{tm95.1(CAG-GCaMP6f)Hze}$/MwarJ) were a kind gift from Dr James W. Putney Jr (National Institute of Environmental Health Sciences). C57BL6/J mice were obtained from the Animal Resources Centre (Western Australia).

Genotyping was performed on mouse toe or ear DNA using the following primers: to distinguish *K5-CreERT2* 5'-GCA AGA CCC TGG TCC TCA C-3', 5'-GGA GGA AGT CAG AAC CAG GAC-3', 5'-ACC GGC CTT ATT CCA AGC-3' (wildtype 322 bp, mutant 190 bp); and to distinguish *TdTomato-fl* and *GCaMP6f-fl* 5'-CTC TGC TGC CTC CTG GCT TCT-3', 5'-CGA GGC GGA TCA CAA GCA ATA-3' and 5'-TCA ATG GGC GGG GGT CGT T-3' (wildtype 330 bp, mutant 250 bp).

To induce expression of GCaMP6f and TdTomato in K5-positive cells, female mice were administered tamoxifen (1.5 mg) diluted in sunflower oil and ethanol (10%) via intraperitoneal injection at 4-weeks of age. A further three tamoxifen injections were administered every second day on alternating sides at 8-weeks of age, providing a total dose of 6 mg per mouse. A 4-6-week washout period was observed before mating. Male mice were injected with 4×1.5 mg tamoxifen injections every second day at 8-weeks of age (total dose 6 mg per mouse). Female experimental mice were mated in pairs or trios with wildtype sires. To obtain mammary tissue during gestation, sires were removed after observation of a copulation plug and mammary tissue harvested 15.5-16.5 days-post-coitus (dpc). To obtain lactating tissue, sires were removed prior to littering and female mice were allowed to nurse for 8-14 days (peak lactation).

Human subjects

Healthy tissue biopsies from consented lactating women (25-33 years old) were obtained from the Susan G. Komen Tissue Bank at the IU Simon Cancer Center (*34*). Tissue donors were recruited under a protocol approved by the Indiana University Institutional Review Board (IRB protocol number 1011003097) and according to The Code of Ethics of the World Medical Association (Declaration of Helsinki), with site-specific approval from the Mater Misericordiae Ltd Human Research Ethics Committee. Breast biopsies were fixed in formalin and paraffin-embedded as per standard protocols. Lactating samples were collected from women who were actively breastfeeding at the time of tissue donation (at least once per day). Donors included in this study had been breastfeeding for 6 to 23 months prior to tissue donation.

Immunohistochemistry

IHC was performed based on a previously published protocol (*35*). Briefly, formalin-fixed paraffin-embedded mouse and human slides were deparaffinized in xylene and rehydrated in a reducing ethanol series. Tissue was permeabilized in phosphate buffered saline (PBS) containing triton X-100 (0.5%). Heat-induced epitope retrieval was performed in sodium citrate (0.01 M, pH 6) for 11 min at 110°C using a NxGen Decloaking Chamber. Slides were blocked in PBS containing normal goat serum (10%) and triton X-100 (0.05%) for 1 h. Primary antibodies were incubated overnight at 4°C in a humidified chamber. The following primary antibodies were used in this study: rabbit anti-SMA (1:200), rabbit anti-MYLK (1:700-1:1000), rabbit anti-CNN1 (1:700-1:1000), rabbit anti-CALD1 (1:200), mouse anti-E-cadherin (1:200-1:400) and chicken anti-K14 (1:200-1:400). Secondary antibodies were incubated for 1 h at room temperature. Nuclei were stained with DAPI dilactate (625 ng/mL) for 10 min at room temperature and tissue was imaged on an Olympus BX63F upright epifluorescence microscope using a UPlanSAPO 20×/0.75 objective lens.

Tissue clearing

Mammary tissue was dissected, spread on foam biopsy pads and optimally fixed in neutral buffered formalin (NBF, 10%) for 3-9 h (according to size) at room temperature. Lacrimal and epididymal tissue was dissected and fixed in NBF for 4-7 h. Pre-stimulation with OT [85 nM (lacrimal and mammary), 850 nM (epididymis), 5-20 min] was performed on live tissue prior to

fixation, as indicated. Tissue clearing was performed on fixed tissue using a modified CUBIC protocol (*15, 36*). Briefly, tissue was immersed in CUBIC Reagent 1A [urea (10% w/w), Quadrol® (5% w/w), triton X-100 (10% w/w), NaCl (25 mM) in distilled water] for 2-3 days at 37°C, washed in PBS and blocked overnight at 4°C in PBS containing normal goat serum (10%) and triton X-100 (0.5%). Tissue was incubated in primary antibodies diluted blocking buffer at 4°C for 4 days. The following primary antibodies and dilutions were used for wholemount immunostaining in this study: rabbit anti-SMA (1:300), chicken anti-K14 (1:200), rabbit anti-pMLC (1:200), chicken anti-GFP (1:1000-1:2000) and rabbit anti-CALD1 (1:200). Secondary antibodies were used at 1:500, incubated for 2 days at 4°C for wholemount immunostaining. Nuclei were stained with DAPI dilactate (5 μg/mL) for 2-3 h at room temperature. Washing was performed in PBS after primary and secondary antibody incubations (3 × 1 h). Tissue was placed in modified CUBIC Reagent 2 [sucrose (44% w/w), urea (22% w/w), triethanolamine (9% w/w), triton X-100 (0.1% v/w) in distilled water] at 37°C and imaged within 1-7 days (*36, 37*). Tissue was imaged in CUBIC Reagent 2 using an Olympus FV3000 laser scanning confocal microscope with UPLSAPO 10×/0.4, UPLSAPO 20×/0.75 and UPLFLN 40×/0.75 objective lenses. Imaging depth (*z*) is recorded from the start of the image sequence, typically 50-150 μm through the cleared structure. Visualization and image processing was performed in Imaris (v9.2.1) or ImageJ (v1.52e, National Institutes of Health) (*38, 39*). Denoising of 3D image stacks was performed as previously described (*40*).

Primary cells

Abdominal and inguinal mammary glands were dissected from pregnant *GCaMP6f-TdTom;K5CreERT2* mice (15.5-16.5 dpc), lymph nodes removed and mammary tissue finely chopped. Cells were isolated using published protocols (*21, 41*). Cells were plated in DMEM/F12 with FCS (10%) on collagen-coated (50 μg/mL) NanoSurface 96-well plates (NanoSurface Biomedical ANFS-0096) and allowed to attach for at least 2.5 h.

Cells were imaged in physiological salt solution [PSS; HEPES (10 mM), KCl (5.9 mM), $MgCl_2$ (1.4 mM), NaH_2PO_4 (1.2 mM), $NaHCO_3$ (5 mM) NaCl (140 mM), glucose (11.5 mM), $CaCl_2$ (1.8 mM); pH 7.3-7.4] within 12 h from the time of sacrifice. Cells were loaded with BAPTA-AM (100 μM, ThermoFisher Scientific, B6769) and EGTA-AM (100 μM, ThermoFisher

Scientific, E1219), as indicated, in complete media at 37°C for 20-40 min before imaging. Pre-treatments with ML-7 (20 µM, Abcam, Ab120848), Y27632 (10 µM, Abmole, M1817) or a combination of ML-7 and Y27632 were performed for 10-20 min in PSS. Cells were imaged on an Olympus FV3000 inverted confocal microscope using a UPLSAPO 30×/1.05 silicone objective, resonant scanner and z-drift compensator. The rise time (T_{peak}) for GCaMP6f is approximately 80 ms; the half decay time ($T_{1/2}$) is 400 ms. Images were acquired every 3 s (< firing duration) for 6 min. Cells were stimulated with OT (0.85 nM) at 30 s; the concentration of ML-7 and Y27632 were maintained for the duration of the assay.

Mammary organoids

Mammary organoids from *GCaMP6f;K5CreERT2* virgin mice were generated as previously described (*21*). Organoids were cultured for 7-10 days, loaded with CellTracker™ Red (1.5 µM) for 20 min at 37°C. Live imaging was performed with OT stimulation (85 nM) on an Olympus FV3000 laser scanning microscope using a resonant scanner and UPLSAPO 30×/1.05 silicone objective.

Live 4D tissue imaging

Mammary tissue was harvested from lactating *GCaMP6f;K5CreERT2* and *GCaMP6f-TdTom;K5CreERT2* mice, diced and loaded with CellTracker™ Red for at least 20 min at 37°C, as indicated (*9*). Lacrimal glands (extraorbital) and epididymides (caput) were isolated from *GCaMP6f-TdTom;K5CreERT2* mice; the epididymal tissue was cut into 2-3 pieces for live imaging. Tissue was stimulated with OT (85 nM, mammary and lacrimal; 850 nM epididymis) in PSS, whilst imaging on an Olympus FV3000 laser scanning microscope using a resonant scanner and UPLSAPO 30×/1.05 silicone objective. Images were acquired every 3-5 s (< firing duration) for 15-30 min.

Registration and analysis of live 4D tissue imaging

We used Advanced Normalization Tools (ANTs, github.com/ANTsX/ANTs) to register the red fluorescence of the live Ca^{2+} imaging to the first time point of each movie (*17*, *18*). We used the following call on each image of the image sequence : antsRegistration -d 2 --float 1 -o [OutImg, OutImg.nii] -n WelchWindowedSinc -w [0.005,0.995] -u 1 -r [FixImg,MovImg, 1] -t rigid[0.1] -

m MI[FixImg,MovImg,1,32, Regular,0.25] -c [1000x500x200x50,1e-7,5] -f 8x4x2x1 -s 2x1x1x0vox -t Affine[0.1] -m MI[FixImg,MovImg,1,32, Regular,0.25] -c [1000x500x200x50,1e-7,5] -f 8x4x2x1 -s 2x1x1x0vox -t SyN[0.05,6,0.5] -m CC[FixImg,MovImg,1,2] -c [100x500x200x50,1e-7,5] -f 8x4x2x1 -s 2x2x1x0vox -v 1. The resulting warps were then applied to the GCaMP6f channel and the resulting registered movies were analyzed using MATLAB. First, we manually selected regions of interests (ROIs) and extracted the fluorescence time series of each channel. The $\Delta F/F_0$ was then computed as described previously (*42*), and all the GCaMP6f peaks with at least a 10% increase in $\Delta F/F_0$ (change in starting fluorescence divided by starting fluorescence), and a correlation to an example GCaMP6f trace above 0.6, were identified. The time of those peaks was used to select a time period of five frames before and ten frames after the peak in both green and red channels, these time traces were then averaged across all identified peaks within and between each mice tissue. The delay between the peaks was also evaluated with the same criteria.

To uncover any potential coordination in the firing pattern, we used a correlation-based approach. We extracted the Ca^{2+} traces from live imaging of gestation stage alveolar units using the CaImAn python package (*43*). A correlation distance matrix was then built between all the identified ROIs, as well as a Euclidean distance matrix between their centroids, for each of the mice analyzed. These were used to either look at the probability distribution of the Euclidean distance for highly correlated (> 0.5) ROIs, or to build a weighted directed graph between these ROIs.

Gene expression analysis

Preprocessed expression count data were obtained from Karsten Bach (*22*) and analyzed using scripts provided by Bach et al., modified to compare the C12 vs C14 clusters and C13 vs C14 clusters using edgeR 3.22.5 in R 3.5.1 (*44*). An R script to generate the differential expression results between these clusters is available at: (https://gist.github.com/adamewing/2819d7e5072aa35632bba7f51236446b). Violin and volcano plots were generated using the seaborn package for python (*45*); zero counts were removed. Scripts are available at:

(https://gist.github.com/adamewing/931cc44d717959073fa5b09078e7e4b3) and (https://gist.github.com/adamewing/90f1f57985a2033f292debb2e2e5b25f) respectively. Gene Set Enrichment Analysis (GSEA) (*46*) was carried out using genes ranked by fold-change.

Primary cell contraction analysis

Images were quantified using a custom ImageJ macro for reproducibility and to eliminate bias. Briefly, cell boundaries were identified by taking the standard deviation of all movement of each cell during acquisition, thresholding and storing the selection area as an ROI. All ROIs were used for measuring intensity of red and green channels for each individual cell and time-point. For cell length measurements, cell ROIs were expanded by two pixels and the region duplicated, and converted to a binary using the Li thresholding algorithm. Individual Feret diameters were measured and recorded for each time-point and ROI. Data was output as .csv files to be further processed (size exclusion < 18 μm or >45 μm), graphed and analyzed. Of the cells that didn't contract (< 5% contr.) with OT (0.85 nM) alone, approximate 35% did not respond with $[Ca^{2+}]_i$; this submaximal OT concentration was selected because it produced cell contraction in the majority of cells, without causing complete loss of cell adhesion. Scripts are available at: https://github.com/nickcondon.

Statistical analysis

Statistical analysis was performed in GraphPad Prism (v7.03). Details of statistical tests used are outlined in each figure legend or supplementary figure legend.
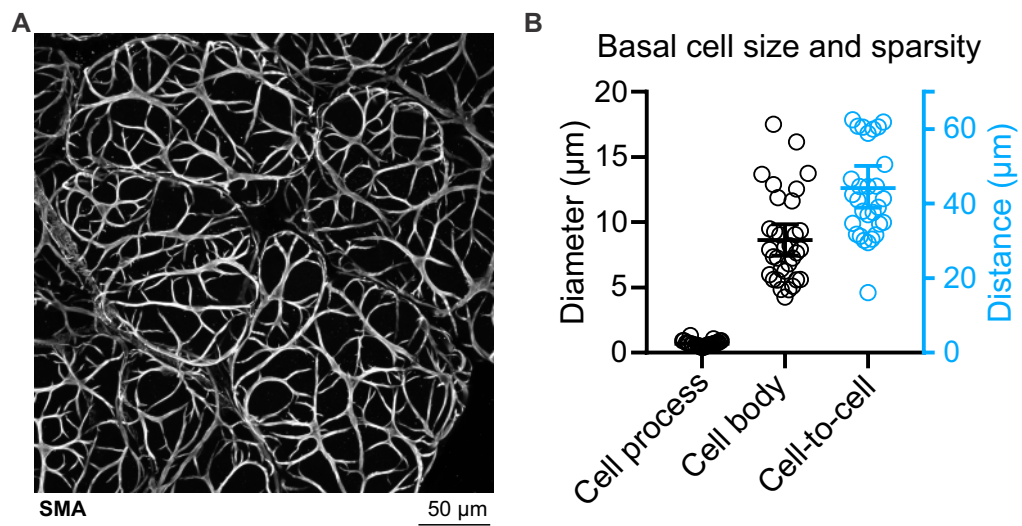
Fig. S1

Fig. S1.

Characterization of morphology and density of mammary alveolar basal cells. (**A**) Maximum intensity z-projection (0-22 μm) of lactating mammary tissue immunostained with smooth muscle actin (SMA) to reveal the cellular morphology and distribution of alveolar basal cells. (**B**) Basal cell diameter at the thinnest cell process and at the cell body (left y-axis). Graph also shows the distance between the body of each basal cell and its closest basal neighbor (right y-axis). Basal cells are separated from their closest neighbor by a distance that is approximately 6× their maximum width. Spatial resolution = 0.3 μm; 33 cells analyzed from n = 3 mice.

Fig. S2

A

B
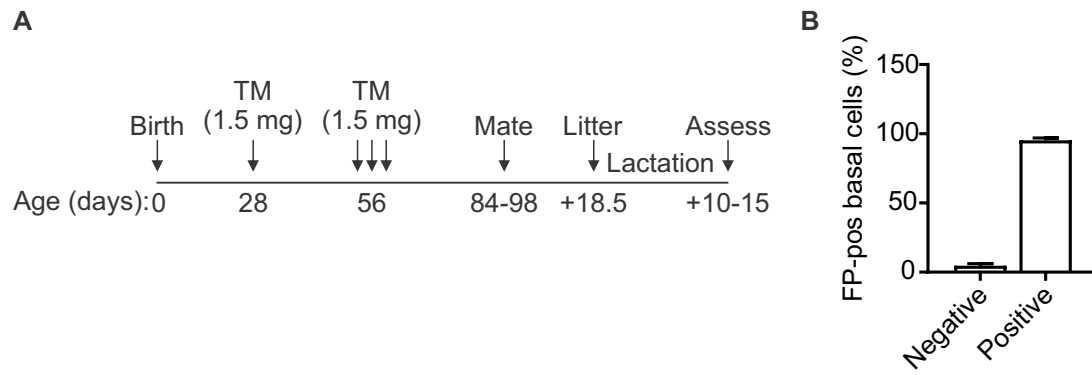
Fig. S2.

Induction and analysis of fluorescent protein (FP) expression in basal cells. (**A**) Schematic representation of the experimental timeline to generate FP-positive lactating tissue. (**B**) The percentage of all basal cells (determined by SMA positivity) that are FP-positive. Positivity was scored from 3D image sequences of cleared tissue; 2400 cells counted from n = 3 mice. TM, tamoxifen.
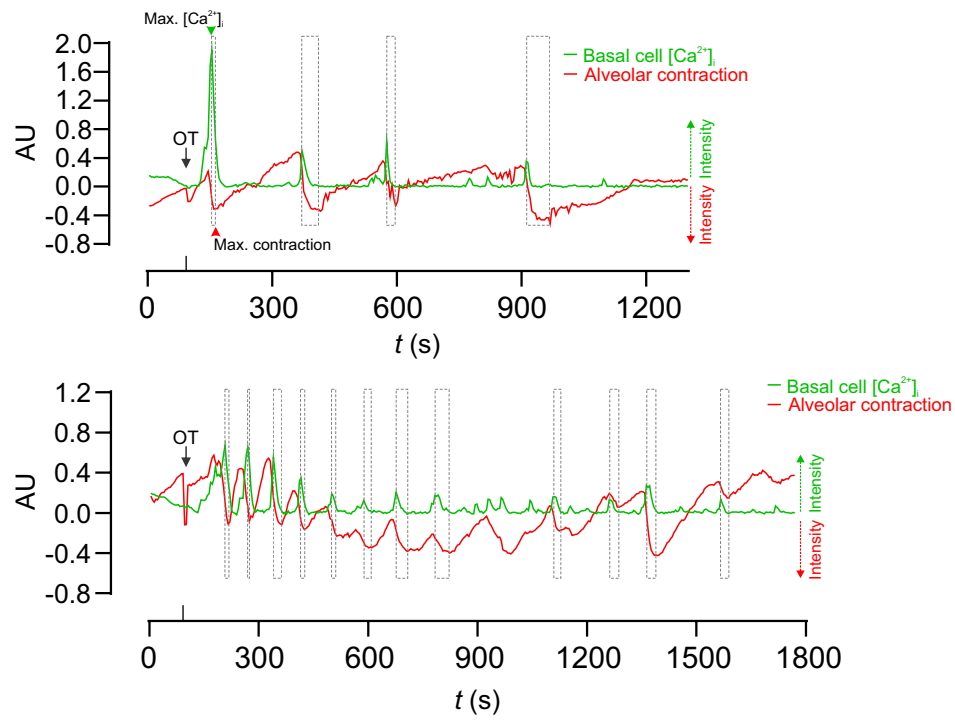
Fig. S3

Fig. S3.

Temporal relationship between $[Ca^{2+}]_i$ responses and alveolar unit contraction. Additional examples (total n = 3 mice, related to Fig. 1) showing $[Ca^{2+}]_i$ responses (green) and alveolar unit contractions (red) in lactating mammary tissue from *GCaMP6f;K5CreERT2* mice. $[Ca^{2+}]_i$ measurements are $\Delta F/F_0$. Alveolar unit contractions are shown by negative deflection (reduction in the intensity of the red fluorescence due to displacement of the alveolar unit). Boxes align with the peak $[Ca^{2+}]_i$ response (left) and the peak contractile response (right). AU, arbitrary unit.
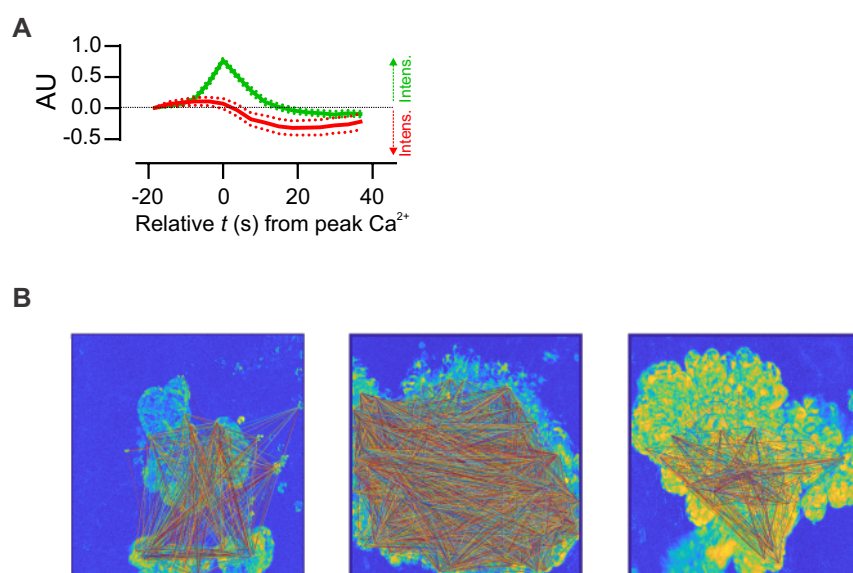
Fig. S4

A

B

Fig. S4.

Ca^{2+}-contraction coupling and tissue-level coordination in _GCaMP6f-TdTom;K5CreERT2_ mice. (**A**) Average peak $[Ca^{2+}]_i$ response (green) and contractile response (red) in mammary tissue isolated from lactating _GCaMP6f-TdTom;K5CreERT2_ mice. $[Ca^{2+}]_i$ measurements are $\Delta F/F_0$. Alveolar unit contractions are shown by negative deflection (reduction in the intensity of the red fluorescence due to contraction/movement of the basal cell). To calculate average ($\pm$ SEM) response, $[Ca^{2+}]_i$ elevations were first identified and fluorescence measurements for 5 frames before and 10 frames after the peak response plotted. Values were averaged from both the first response and the oscillatory phase; n = 3 mice. (**B**) Graph theory showing connection between highly correlated responses; n = 3 mice (gestation). AU, arbitrary unit.
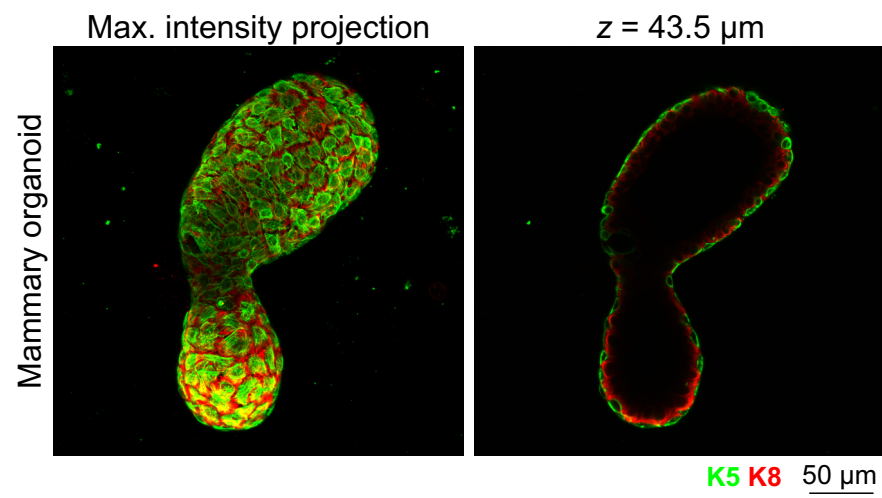
Fig. S5

K5 K8   50 μm

Fig. S5.

Correct cellular organization and lineage-marker expression in mammary organoids.
Mammary organoids created from non-pregnant mice were immunostained with the basal cell marker K5 (green) and the luminal cell marker K8 (red). Images show maximum intensity z-projection (0-54 μm) and a single optical plane.
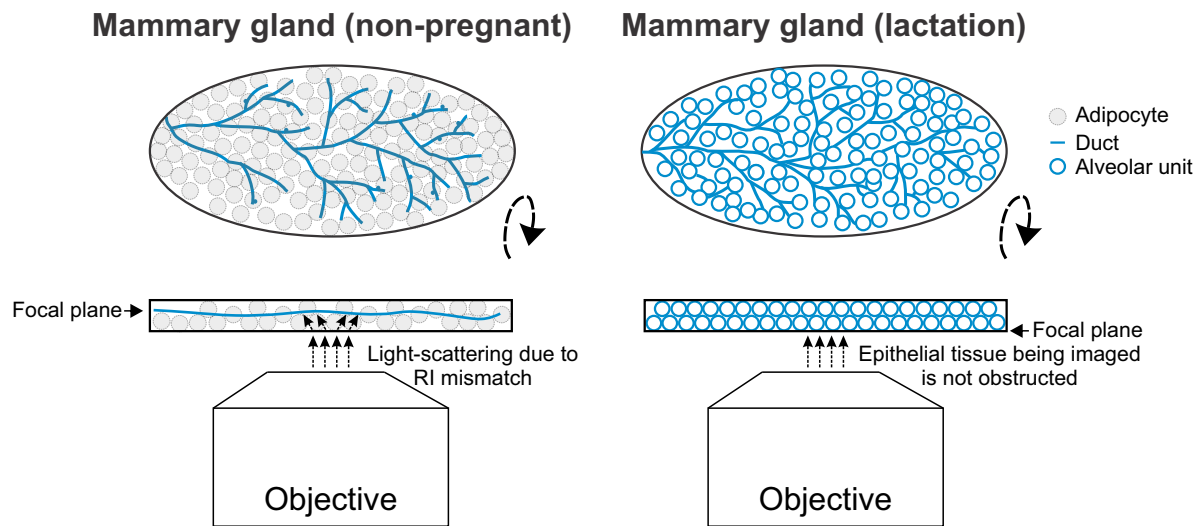
Fig. S6

Fig. S6.

Technical challenges impeding $[Ca^{2+}]_i$ measurements in live mammary tissue from non-pregnant mice. In the non-pregnant gland, mammary epithelial cells are organized in a branching ductal tree that is embedded deep within an adipocyte-rich (light scattering) stroma. In contrast, the abundance of epithelial structures and the relative lack of adipocytes in the pregnant and lactating mammary gland, make these developmental stages more conducive to live $[Ca^{2+}]_i$ imaging. RI, refractive index.
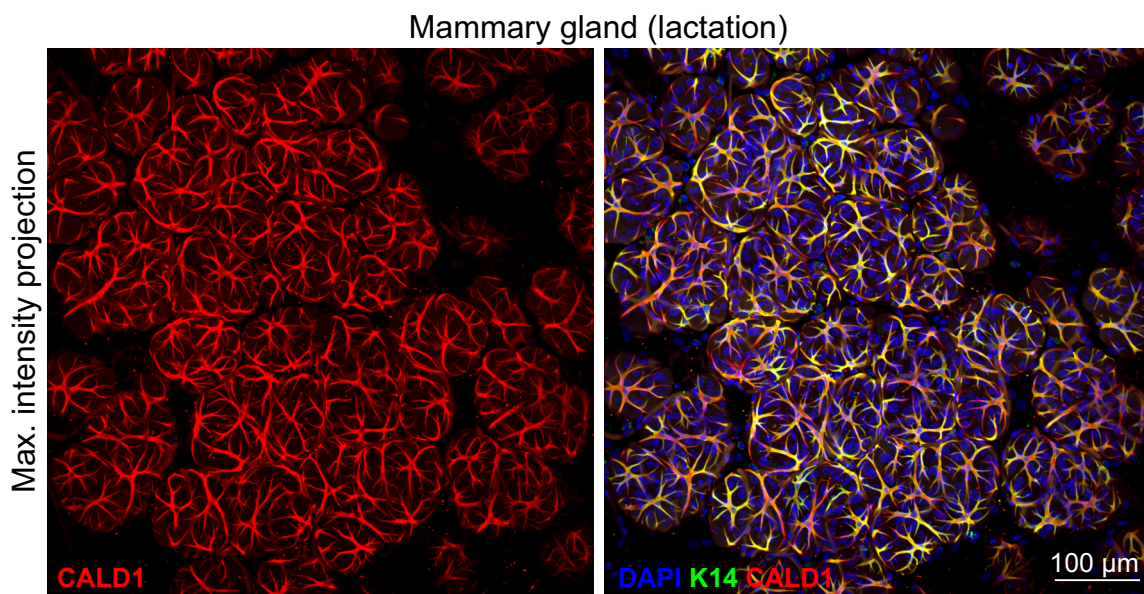
Fig. S7

Mammary gland (lactation)

Fig. S7.

CALD1 expression in lactating mammary tissue. Maximum intensity z-projection (0-20 μm) of cleared mammary tissue immunostained with K14 (green) and CALD1 (red). Nuclei (DAPI) are blue.
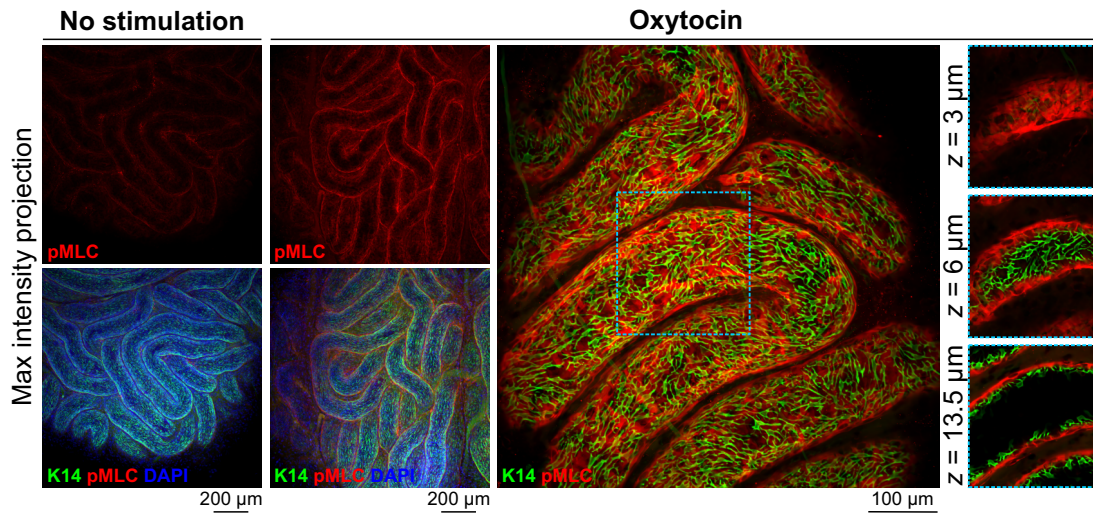
Fig. S8

Fig. S8.

Detection of activated myosin in epididymal tissue. Maximum intensity z-projections of cleared epididymal tissue immunostained with K14 (green) and pMLC (red). Tissue was stimulated with OT (850 nM) 20 min prior to fixation, as indicated. Nuclei (DAPI) are blue; n = 3 mice.

Movie S1.

OT response in live mammary tissue isolated from lactating *GCaMP6f;K5CreERT2* mice. GCaMP6f (green) and CellTracker™ (red). OT was added at 01:33 (min:s), as indicated. Total movie length is 29:30. Related to Fig. 1.

Movie S2.

OT response in live mammary tissue isolated from lactating *GCaMP6f-TdTom;K5CreERT2* mice. GCaMP6f (green) and TdTomato (red). OT was added at 01:09 (min:s), as indicated. Total movie length is 23:03. Related to Fig. 2.

Movie S3.

OT response in live mammary organoids isolated from non-pregnant *GCaMP6f;K5CreERT2* mice. GCaMP6f (green) and CellTracker™ (red). OT was added at 00:45 (min:s), as indicated. Total movie length is 27:00. Related to Fig. 3.

Movie S4.

OT response in live mammary (alveolar) tissue isolated from pregnant (15.5-16.5 dpc) *GCaMP6f-TdTom;K5CreERT2* mice. GCaMP6f (green) and TdTomato (red). OT was added at 00:38 (min:s), as indicated. Total movie length is 25:08.

Movie S5.

OT response in live mammary (ductal) tissue isolated from pregnant (15.5-16.5 dpc) *GCaMP6f-TdTom;K5CreERT2* mice. GCaMP6f (green) and TdTomato (red). OT was added at 01:15 (min:s), as indicated. Total movie length is 26:13. Related to Fig. 4.

Movie S6.

OT response in live mammary (ductal) tissue isolated from lactating *GCaMP6f-TdTom;K5CreERT2* mice. GCaMP6f (green) and TdTomato (red). OT was added approximately 00:45 (min:s) prior to imaging. Total movie length is 26:13.

Movie S7.

OT response in live primary cells isolated from pregnant (15.5-16.5 dpc) *GCaMP6f-TdTom;K5CreERT2* mice and grown on a nanopatterned surface. OT was added at 00:27 (min:s), as indicated. Total movie length is 06:00. Related to Fig. 5.

Movie S8.

OT response in live primary cells isolated from pregnant (15.5-16.5 dpc) *GCaMP6f-TdTom;K5CreERT2* mice, grown on a nanopatterned surface and pre-treated with BAPTA-AM for 30 min. OT was added at 00:27 (min:s), as indicated. Total movie length is 06:00. Related to Fig. 5.

Movie S9.

OT response in live lacrimal tissue isolated from *GCaMP6f-TdTom;K5CreERT2* mice. GCaMP6f (green) and TdTomato (red). OT was added at 00:45 (min:s), as indicated. Total movie length is 15:55. Related to Fig. 6.

Movie S10.

OT response in live epididymal tissue isolated from *GCaMP6f-TdTom;K5CreERT2* mice. GCaMP6f (green) and TdTomato (red). OT was added at 01:38 (min:s), as indicated. Total movie length is 25:48. Related to Fig. 6.